Ultrasound-assisted aberration correction of transcranial photoacoustic imaging based on angular spectrum theory

Qiuqin Mao, Yingjie Feng, Chao Tao [*], Xiaojun Liu

Ministry-of-Education Key Laboratory of Modern Acoustics, Department of Physics, Collaborative Innovation Center of Advanced Microstructures, Nanjing University, Nanjing 210093, China

ARTICLE INFO

ABSTRACT

To correct the refraction aberration induced by the skull in photoacoustic imaging, a method for phase distortion compensation is proposed based on the angular spectrum theory with the aid of ultrasonic signals. This method first updates the speed of sound distribution by iteratively performing aberration correction in the ultrasonic reconstruction. Then the speed of sound distribution obtained with ultrasound-assisted serves as prior knowledge to address phase distortion compensation by adjusting the phase shift factor of the wavefront in different media. Finally, the aberration-corrected ultrasonic-photoacoustic dual-modality image can be obtained. Numerical simulations and phantom experiments confirm the effectiveness of this method. Specifically, in simulations, the position error of the proposed method is reduced from −13.61 % to 1.27 % in depth compared to the method based on the reconstruction with constant speed. Moreover, a real ex-vivo rabbit skull experiment illustrates the potential biological application of the proposed method in transcranial photoacoustic imaging.

1. Introduction

Transcranial imaging is a pivotal technique for elucidating brain function and detecting brain diseases [1,2]. Among current imaging modalities, x-ray computerized tomography poses challenges due to prolonged exposure to ionizing radiation [3]. Magnetic resonance imaging is hindered by its high cost, limiting its widespread use [4]. Ultrasound (US) imaging, while non-ionizing, is constrained by its limited ability to differentiate soft brain tissues based on acoustic impedance contrast [5]. Recently, photoacoustic (PA) imaging has emerged as a promising modality for capturing both structural and functional brain images in animal studies [6,7].

PA imaging, a non-invasive and non-ionizing hybrid technique, merges optical contrast with ultrasound resolution [8]. In PA imaging, tissue absorbs electromagnetic waves emitted by a short-pulsed laser beam, leading to thermoelastic expansion and contraction, thereby generating acoustic waves [9,10]. Reconstruction algorithms process the received acoustic waves to form images of absorbers. Compared to US imaging, PA imaging benefits from higher optical contrast due to optical property inhomogeneity [11,12].

In transcranial PA imaging, a key challenge is the significant acoustical impedance mismatch between soft tissue and the skull [13, 14]. The intricate propagation of acoustic waves through the skull involves transmission, reflection, refraction, scattering, attenuation, broadening, etc. [15,16]. These complex propagations lead to phase distortion. Images reconstructed by methods based on constant speed or the straight-ray propagation assumption have substantial image aberration due to phase distortion [17]. Numerous approaches have been proposed to effectively address skull-induced acoustic aberrations [18, 19]. Many researches focus on obtaining more precise time-of-flight (TOF) approximations by considering non-straight rays [15,20–23]. The prior knowledge of the speed of sound (SOS) can be obtained through other modal imaging modalities, such as US with PA method [24,25] and x-ray computed tomography with PA method [19,26]. However, TOF approximation often involves complex calculations of refraction angles and paths in the time domain. Another strategy involves employing mathematical model-based reconstruction methods based on the elastic wave equation for aberration correction [26–29]. While these methods can yield more accurate estimates of acoustic properties, they tend to be computationally intensive due to iterative processes. Additionally, deep learning techniques have been proposed to correct distorted PA signals by minimizing the error between predicted

and actual models [30,31]. Though the deep learning method indeed improves image quality, its effectiveness highly hinges on the quality of training data. Moreover, this data-driven deep learning approach lacks robust interpretability of the results [32].

In this work, a method for phase distortion compensation based on the angular spectrum theory is introduced for skull-refracted aberration correction in transcranial PA imaging. The proposed method realized in the frequency wavenumber domain integrates ultrasound with photoacoustic dual modalities imaging to correct strongly refracted aberrations in transcranial PA images. The proposed method is independent of the geometry of the skull when dealing with refraction. The phase distortion caused by the skull refraction is compensated by adjusting the phase shift factor according to the SOS of the medium. Thus, the proposed method can effectively avoid the complex calculation of refraction angles and refraction paths in the method based on ray tracing when encountering irregular interfaces of the skull. The realization in the frequency wavenumber domain can be effective and efficient in getting the SOS distribution and aberration-free images in the US. Then aberration correction of PA images can be assisted by the prior knowledge of the SOS distribution obtained by aberration-free US images. The efficacy of this method is validated through numerical simulations, with further validation conducted via experiments on phantoms and real *ex vivo* skull experiments to demonstrate its practical applicability.

2. Method

In the angular spectrum theory of homogeneous media, any wave surface can be decomposed into the sum of plane waves propagating in different directions [33,34]. The angular spectrum formed by these plane waves can be recombined to obtain the angular spectrum of the next depth by the transfer function. This transfer function takes into account the phase change that each plane wave will experience on its way to the next depth. That is, in the 2D homogeneous medium shown in Fig. 1(a), the wavefield at the next depth $z+\Delta z$ can be obtained by phase shifting the wavefield at any depth z.

To realize the wavefield exploration in a homogeneous media with the constant speed of sound (SOS), let's suppose the detected upward propagating wavefield is denoted $p(x, z, t)$. The angular spectrum of the detected wavefield can be obtained by performing a 2D Fourier transform of $p(x, z, t)$ on x and time t. Then, the resulting angular spectrum at depth z is multiplied by a phase shift factor $\alpha_c(k_x, \Delta z, \omega)$ to obtain the angular spectrum at the next depth $z+\Delta z$. Finally, based on the 2D inverse Fourier transform, the wave field $p(x, z+\Delta z, t)$ can be achieved with condition $t = 0$, expressed as [35]:

$$p\left(x, z+\Delta z, t\right) = \mathscr{F}_{k_x,\omega}^{-1}\left[\mathscr{F}_{x,t}(p(x,z,t))\alpha_c\left(k_x, \Delta z, \omega\right)\right], \qquad (1)$$

with

$$\alpha_c\left(k_x, \Delta z, \omega\right) = e^{j\text{sign}(\omega)\sqrt{\frac{\omega^2}{c^2}-k_x^2}\Delta z}, \qquad (2)$$

where $\mathscr{F}_{x,t}$ represents the 2D Fourier transform on x and t, and $\mathscr{F}_{k_x,\omega}^{-1}$ represents the 2D inverse Fourier transform on k_x and ω, j in the phase shift factor is the imaginary unit, ω is the angular frequency, k_x is the wavenumber in the x-direction. The sign($\bullet$) is the sign function, and c is the SOS of the medium. Eqs. (1)-(2) said that the initial pressure field in the region of interest $z+\Delta z$ in Fig. 1(a) can be reconstructed by phase shift layer-wise along the depth from the detection surface at depth z.

However, due to the mismatch in acoustic impedance between the skull and surrounding tissues, the transcranial PA model [Fig. 1(b)] is a heterogeneous scene. Strong refraction occurs at the skull interface, which means that the propagation direction of the wave changes. If phase shift is performed based on the assumption of constant speed, the reconstructed image will suffer from severe aberration.

To perform phase compensation more accurately, the SOS distribution in the entire imaging area needs to be considered. As shown in the red dashed line in Fig. 1(b), the SOS $c(x, z)$ is a function both of x and z. The phase shift factor independent of the 2D Fourier transform ($\mathscr{F}_{x,t}$) in Eq. (1) should be included in the 1D Fourier transform of x ($\mathscr{F}_x$). Then, for the scenario in which the lateral velocity varies, the wavefield extrapolation should be expressed as [36]:

$$p'\left(x, z+\Delta z, t\right) = \mathscr{F}_{k_x,\omega}^{-1}\left\{\mathscr{F}_x\left[\mathscr{F}_t(p(x,z,t))\alpha_{c(x,z)}\left(k_x, \Delta z, \omega\right)\right]\right\}, \qquad (3)$$

with

$$\alpha_{c(x,z)}\left(k_x, \Delta z, \omega\right) = e^{j\text{sign}(\omega)\sqrt{\frac{\omega^2}{c^2(x,z)}-k_x^2}\Delta z}. \qquad (4)$$

The implementation of Eq. (3) can be realized based on the piecewise integration along the x direction. This shows that the wave field of the depth $z+\Delta z$ can be obtained by superposition after different phase shifts of the wave field at depth z according to the corresponding SOS at depth $z+\Delta z$. In Fig. 1(b), the transcranial model is simplified as a three-layer transmission process with two different SOS. Then the piecewise integration of Eq. (3) can be achieved by two piecewise phase shifts. Assuming the surrounding soft tissue [blue background in Fig. 1(b)] and the skull [orange background in Fig. 1(b)] have a speed of sound of c_1 and c_2, respectively. A window function distribution related to $c(x, z)$ is used to segment the input wavefield along the x direction corresponding to distinct SOS. Therefore, the initial wave field $p'(x, z+\Delta z, t)$ at depth $z+\Delta z$ can be obtained by a linear superposition after two piecewise phase shift operations. The calculation can be expressed as:
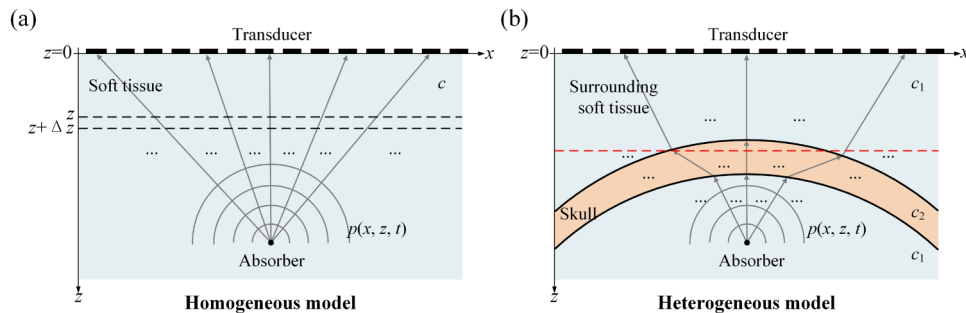

Fig. 1. Schematic illustration of forward photoacoustic wave propagation in (a) the homogeneous and (b) heterogeneous three-layered skull model. The gray line with an arrow indicates the propagation path of the wave.

$$p'\left(x, z+\Delta z, t\right) = \mathscr{F}_{k_x,\omega}^{-1}\left\{\sum_{i=1,2}\mathscr{F}_x[w_i(x, z+\Delta z)\mathscr{F}_t(p(x,z,t))]e^{jsign(\omega)\Delta z\sqrt{\frac{\omega^2}{c_i^2}-k_x^2}}\right\},$$

(5)

where the window function distribution is defined as:

$$w_i\left(x, z\right) = \begin{cases} 1 & \text{if} \quad c(x,z)=c_i \\ 0, & \text{others} \end{cases}$$

(6)

Therefore, the specific reconstruction process can be obtained by extrapolating the wave field $p(x, z = 0, t)$ received at depth $z = 0$ downward by Δz according to Eqs. (5)-(6). Each extrapolation will get the initial pressure result at the corresponding depth layer. When the extrapolation reaches the required imaging depth, the results of all layers are combined to get the image of the region of interest.

To realize the phase shift in the transcranial PA imaging, it is necessary to know the SOS distribution map $c(x, z)$ of the imaging region in advance for input. Since the US image can clearly distinguish the position where changes in acoustic impedance, the SOS distribution can be obtained with the assistance of US signals. However, the reconstruction of the transcranial US image is also a heterogeneous scenario. Thus, aberrations in the US image first need to be corrected to update the SOS distribution. Based on the above derivation of wavefield extrapolation in heterogeneous scenes, Eqs. (3)-(6) can also be used for aberration correction of US images. Considering the two-way transmission of the wave in the US pulse-echo mode, the SOS implemented in Eqs. (3)-(6) for US image reconstruction uses half of the true SOS. Fig. 2 shows the flow chart of SOS distribution estimation for PA image aberration

correction of the multilayer region of interest.

As shown in Fig. 2, the interface of the skull in Fig. 1(b) can be identified by iterating the US images twice to update the SOS distribution. First, based on constant SOS c_1, by performing Eqs. (3)-(6) on the original US signal, the conventional US image without aberration correction can be obtained. In the conventional US image, the result above the upper interface of the skull is accurate while that below the upper interface has image aberration. Extracting the upper interface (the 1st interface) can be used to first update the SOS distribution. Due to the gray difference between the skull interface and the background in the US image, the skull interface can be extracted by using the edge extraction operator based on the gradient of the image. Then the SOS distribution can be updated to $c^{(1)}(x, z)$ by setting c_1 above and c_2 below the upper interface. Second, according to the updated SOS distribution $c^{(1)}(x, z)$, the US image is reconstructed again by performing Eqs. (3)-(6) on the original US signal. In this image, the result above the lower interface of the skull is aberration-free. The lower interface (the 2nd interface) can be extracted by again using the edge extraction operator. Thereby, the SOS distribution of the entire imaging region is updated to $c^{(2)}(x, z)$ with c_1 for the tissue above and below the skull, and c_2 for the skull. Finally, according to the SOS distribution $c^{(2)}(x, z)$, the PA image can be reconstructed by using Eqs. (3)-(6).

In general, the proposed method can achieve corresponding phase compensation for wave surfaces in different media. The effective compensation of phase has the potential to solve the wavefront phase distortion caused by skull refraction. In addition, the proposed method iteratively performs aberration correction on the US image to update the SOS distribution. The updated SOS can bring more accurate aberration correction for subsequent PA reconstruction. Besides, the phase shift in
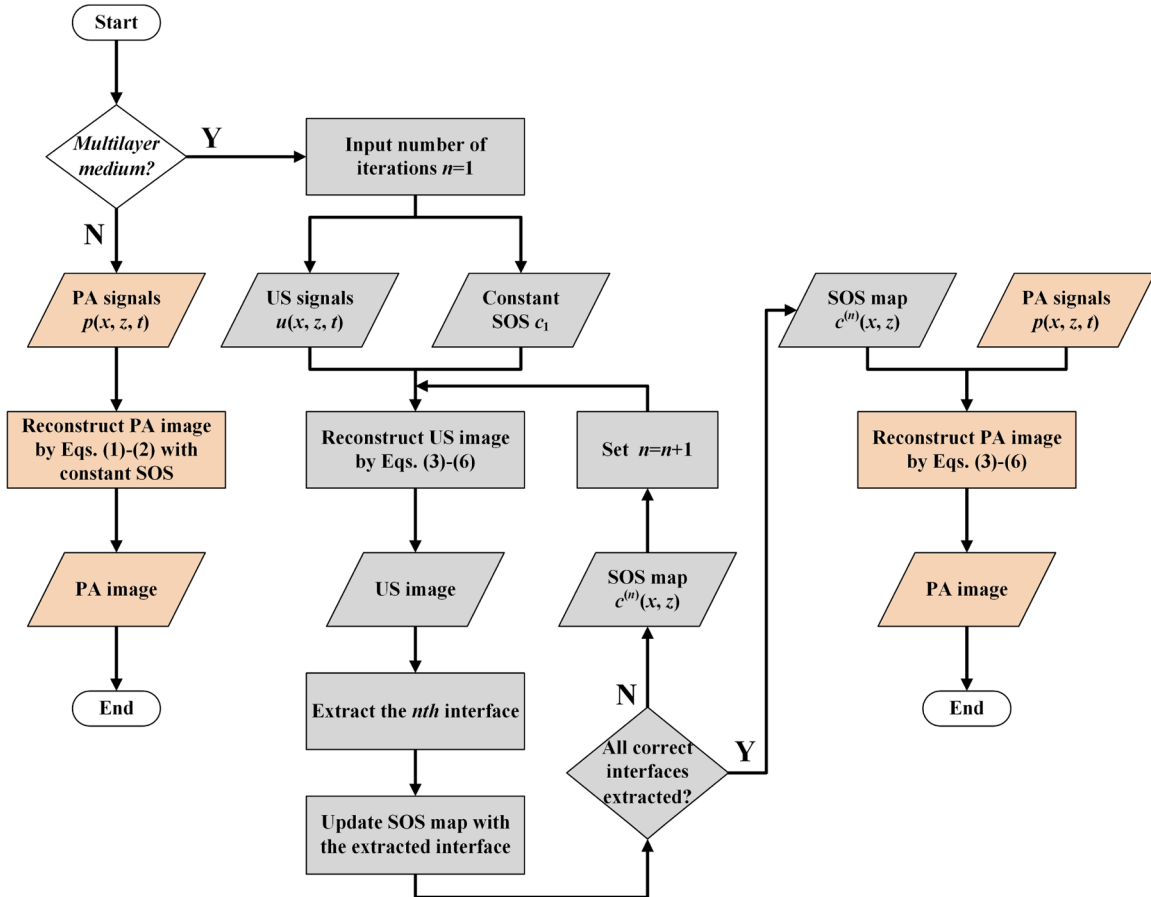

Fig. 2. Flow chart of SOS distribution estimation for PA image aberration correction by using US signals. The gray data flow represents the ultrasonic data flow. Orange represents the photoacoustic data flow.

the frequency wavenumber domain avoids the complex calculation of the time shift in the time domain, which causes a low computational complexity of the proposed method.

3. Numerical simulation

To more clearly understand the impact of the skull on PA image reconstruction, simulations without and with a skull were implemented. The forward model in 2D of the acoustic simulation is conducted through the k-Wave toolbox [37]. The homogeneous medium in the simulation [Fig. 3(a)] has a longitudinal SOS of 1500 m/s and a density of 1000 kg/m³. In Fig. 3(a), seven absorbers (No. 1–7) are distributed at three depths with an interval of 2 mm. A linear array transducer with 64 elements is set 15.5 mm above the absorbers to receive PA signals. The pitch of the element is 0.3 mm. The center frequency of the transducer is 5 MHz.

Fig. 3(b) gives the reconstructed image of absorbers in the homogeneous medium by using the delay-and-sum (DAS) method according to the constant SOS (CS) of 1500 m/s. Since the PA signals only pass through a single homogeneous medium, Fig. 3(b) can well reflect the correct position of the absorber without image aberration.

The heterogeneous simulation with a skull present is shown in Fig. 4 (a). The skull layer [white region in Fig. 4(a)] is considered isotropic with a longitudinal SOS of 2800 m/s and a density of 1900 kg/m³. The medium surrounding the skull [blue in Fig. 4(a)] has a longitudinal SOS of 1500 m/s and a density of 1000 kg/m³. The skull layer is set 9.5 mm below the transducer. The skull layer has a thickness of 5 mm. The skull has a curved geometry. The setting of the absorbers and the transducer are the same as that in the homogeneous simulation. These absorbers are respectively 1 mm, 3 mm, and 5 mm away from the lower interface of the skull.

Fig. 4(b) shows the PA image of absorbers under the skull reconstructed by using DAS with the constant SOS of 1500 m/s. It can be seen that the shape and position of the absorber in Fig. 4(b) are far from the real case. Taking absorber (No. 2) as an example, the position errors in the lateral and depth directions can reach 3.08 % and −13.61 %, respectively. This is because reconstruction at a constant SOS can not compensate for the phase distortion caused by the refraction of the skull. These serious image aberrations make precise localization of the absorbers difficult in the image reconstructed with constant SOS.

Fig. 4(c)-(f) show the process of extracting SOS map from US signals. The US images are all obtained by the angular spectrum shift method [35,38]. Fig. 4(c) is the US image reconstructed with a constant SOS of 1500 m/s. The upper interface [red dashed line] of the skull is extracted from Fig. 4(c) and the SOS map is updated [Fig. 4(d)]. Then, the US image is reconstructed again by using the updated SOS map of Fig. 4(d).
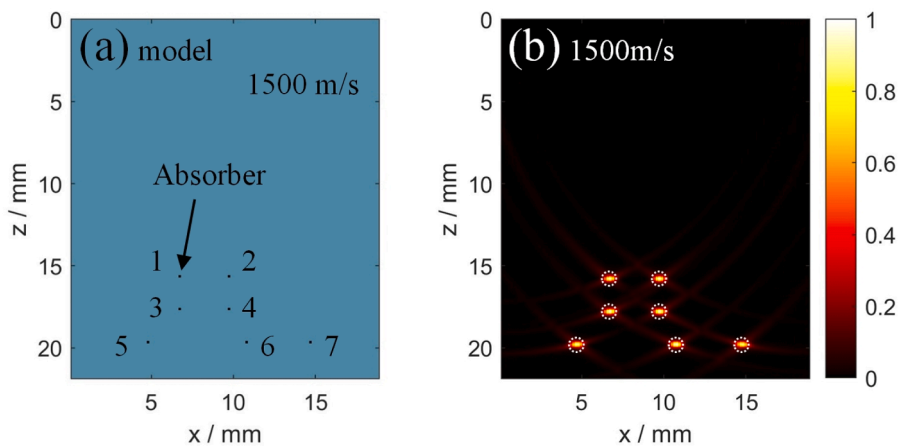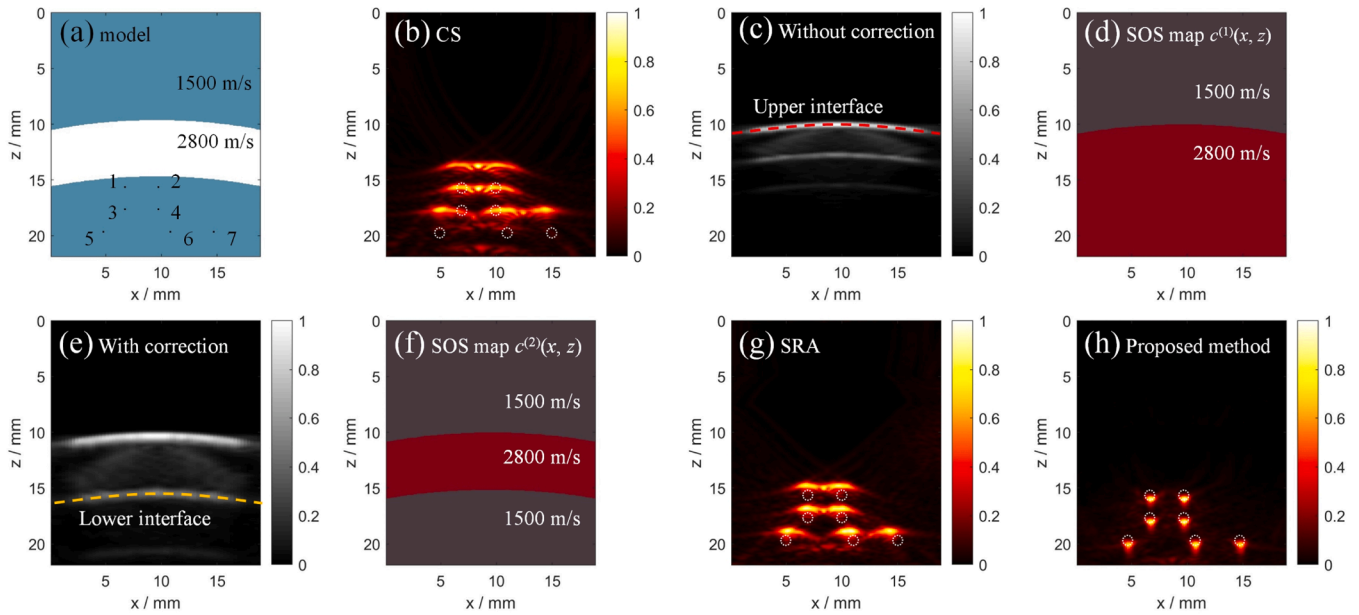
Fig. 4(e) gives the reconstructed US image. From Fig. 4(e), the lower interface [orange dashed line] of the skull is extracted and the final SOS map is updated again, as shown in Fig. 4(f). The extracted SOS map in Fig. 4(f) is almost the same as the SOS map in Fig. 4(a). This verifies the effectiveness of the proposed method in obtaining the SOS map by iterating the US image.

Fig. 4(h) displays the PA image reconstructed by the proposed method. For the sake of comparison, the PA image is also reconstructed by using the straight rays assumption (SRA) method [39], as shown in Fig. 4(g). Both images are reconstructed based on the same SOS map given in Fig. 4(f). It can be seen that the image aberration of the image obtained by the SRA method [Fig. 4(g)] is weaker than that obtained by the CS method [Fig. 4(b)]. The position errors of the absorber (No. 2) in the lateral and depth directions in Fig. 4(g) are reduced to 1.54 % and −6.33 %, respectively. The SRA method can reduce the phase distortion by considering the SOS variation, however, the image [Fig. 4(g)] still has image aberration due to the SRA method ignoring the changes in propagation direction caused by refraction. Compared with the SRA method, the proposed method can better improve image aberration, as shown in Fig. 4(h). The shape and position of the absorbers are closer to the real case [Fig. 3(b)]. The position errors of the absorber (No. 2) in the lateral and depth directions are reduced to 0 % and 1.27 %, respectively. It is said that the proposed method provides more efficient phase distortion correction by considering different phase shifts of refracted wave-surface.

Additionally, imaging results that compensated for the time delay by adjusting the single SOS in the CS method are given to compare the compensation performance with the proposed method. The results by time delay tunning are shown in Fig. 5(a)-(h). The structural similarity index measure (SSIM) [40] is introduced to quantitatively evaluate the similarity between the reconstructed images with the skull and without the skull. The larger the value of SSIM is, the more similar the overall quality of the reconstructed image is to the result without aberration. By comparing the overall image quality with Fig. 3(b), the SSIM of the results with correction [Fig. 4(b), Fig. 4(g)-(h), Fig. 5(a)-(h)] is given in Table 1. It can be seen from Table1 that the SSIM obtained by the proposed method is higher than that obtained by the CS method and the SAR method. These results demonstrate that the image obtained after the aberration correction by the proposed method is closer to the aberration-free imaging result, which confirms the effectiveness in correcting refraction aberration caused by the skull of the proposed method.

By considering the attenuation of the skull, the results reconstructed by the proposed method and the original radio-frequency (RF) signal at the 32nd channel under different attenuation of the skull in 3 dB/(MHz•cm), 6 dB/(MHz•cm), and 12 dB/(MHz•cm) are given in Fig. 6

Fig. 3. Numerical simulation of homogeneous model. (a) The homogeneous model with seven-point absorbers. (b) PA image reconstructed by using DAS at a constant speed of 1500 m/s. White dashed circles in the PA image reveal the real position of absorbers.

Fig. 4. Numerical simulation of the heterogeneous model. (a) Skull model with seven-point absorbers. (b) PA image reconstructed by using DAS at a constant speed of 1500 m/s. (c) US image reconstructed by using DAS at 1500 m/s. (d) Updated SOS map $c^{(1)}(x, y)$ according to the interface of (c) based on the proposed method. (e) US image corrected by the proposed method with the SOS map of (d). (f) Updated SOS map $c^{(2)}(x, y)$ according to the interface of (e) based on the proposed method. (g) PA image reconstructed by SRA method with the SOS map of (f). (h) PA image reconstructed by the proposed method with the SOS map of (f). White dashed circles in the PA image reveal the real position of absorbers.
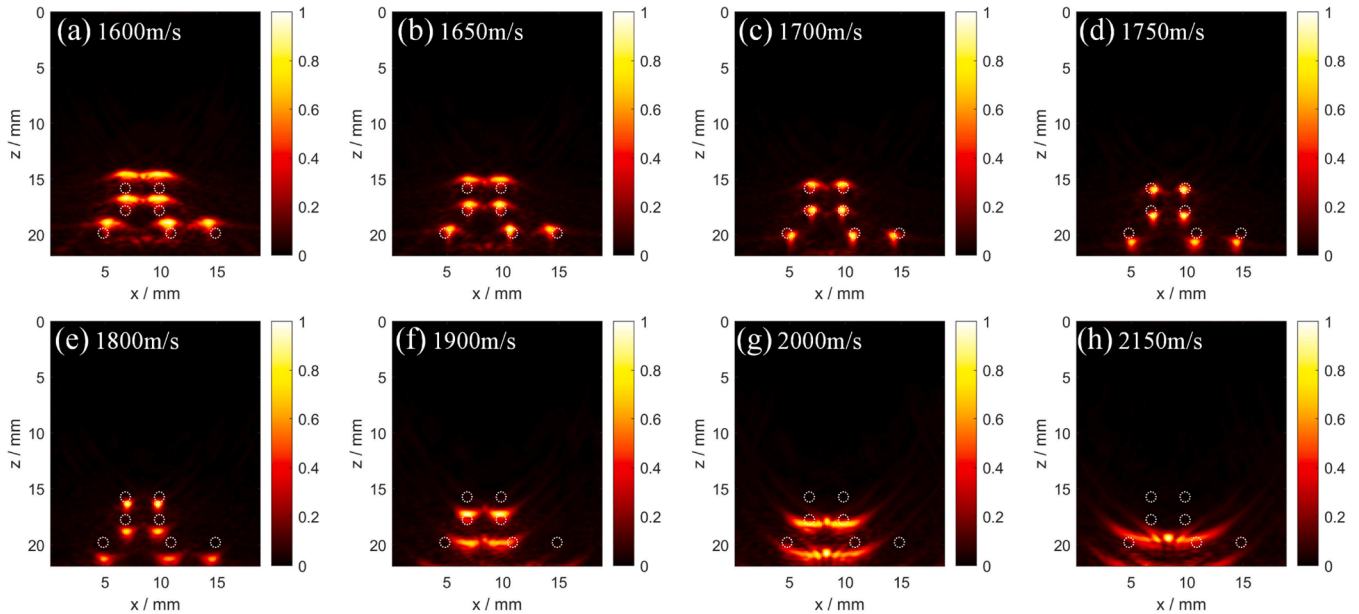
Fig. 5. Images reconstructed by time delay tunning with a constant speed of (a) 1600 m/s, (b) 1650 m/s, (c) 1700 m/s, (d) 1750 m/s, (e) 1800 m/s, (f) 1900 m/s, (g) 2000 m/s, and (h) 2150 m/s. White dashed circles in the PA image reveal the real position of absorbers.

Table 1
SSIM results compared with images without aberration.

Method	CS (km / s)									SRA	Proposed method
	1.5	1.6	1.65	1.7	1.75	1.8	1.9	2.0	2.15		
SSIM	0.48	0.52	0.61	0.67	0.68	0.67	0.62	0.58	0.59	0.54	0.71

(a)-(c). Both the US RF signal and the PA RF signal were normalized, and the overall amplitude of the PA signal was shifted downward by 2 units to be presented in the same coordinate system as the US. In addition, background Gaussian white noise with the different signal-to-noise ratio (SNR) is added while simultaneously considering attenuation in the skull. The SNR is obtained by calculating the ratio of the average power
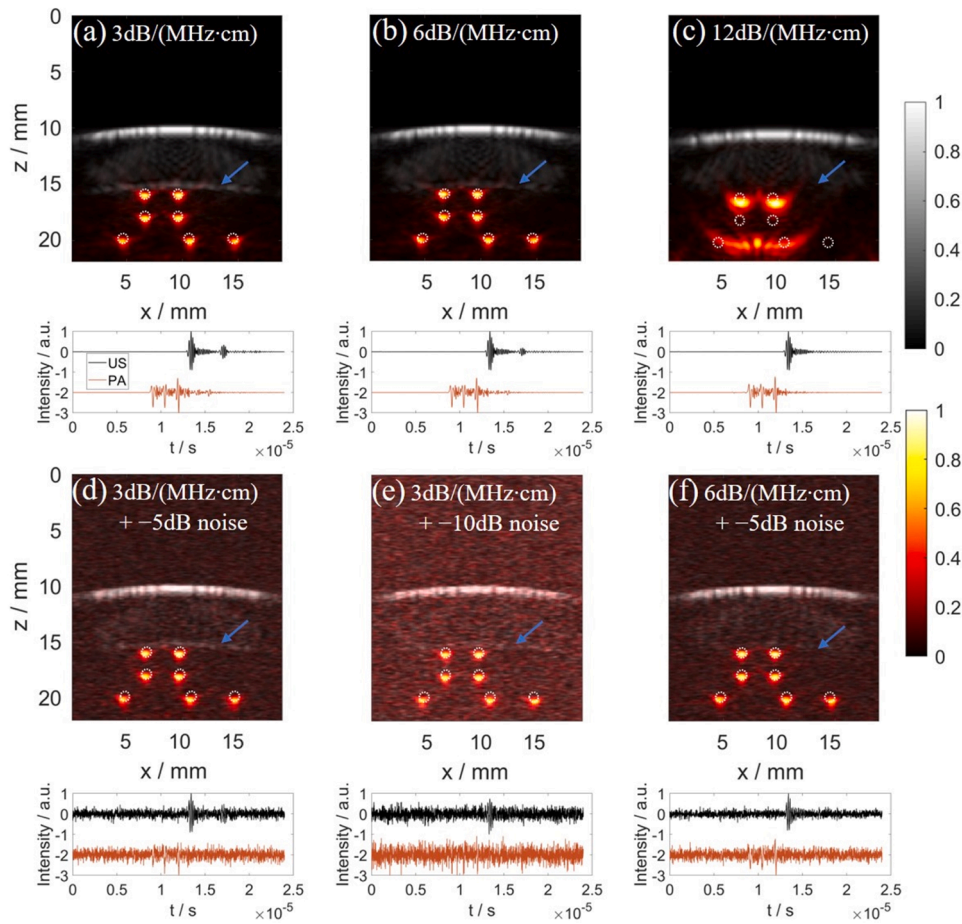
Fig. 6. Images reconstructed by the proposed method and the original RF signal by considering the attenuation in the skull and background noise. Attenuation of (a) 3 dB/(MHz•cm), (b) 6 dB/(MHz•cm), and (c) 12 dB/(MHz•cm) in the skull and without background noise. Attenuation of 3 dB/(MHz•cm) in the skull and noise in the background with an SNR of (d) −5 dB and (e) −10 dB. (f) Attenuation of 6 dB/(MHz•cm) in the skull and noise in the background with an SNR of −5 dB. The blue arrow points to the inner interface of the skull.

of the signal to the average power of the background noise. The equation of the SNR is defined as $10 \times \log_{10}(P_{s\text{-ave}}/P_{b\text{-ave}})$, where $P_{s\text{-ave}}$ and $P_{b\text{-ave}}$ are the average power of the signal and the average power of the background noise, respectively. The reconstruction results with noise and the original RF signals are shown in Fig. 6(d)-(f). The measured SNR of the original signals between the inner interface of the skull and the background in Fig. 6 is 21.94 dB, 16.03 dB, × dB, 9.90 dB, 5.03 dB, and 1.93 dB, respectively. As can be seen from Fig. 6, as the SNR decreases, the grayscale value of the inner boundary of the skull gradually decreases. Especially in Fig. 6(c), due to the large acoustic attenuation, the signal of the inner boundary can not be received by the transducer. Thus the inner boundary can not be effectively reconstructed and extracted in the US image to distribute the SOS. The reconstructed PA image in Fig. 6 (c) is the result of depending on only extracting the upper boundary to distribute the SOS. Due to the incorrect SOS distribution, the PA result in Fig. 6(c) can not reflect the true position of the absorbers. This shows the proposed method has limitations when the inner boundary cannot be extracted. However, in addition to the other figures of Fig. 6(c), since the grayscale value of the inner boundary can still be distinguished from the background noise, the proposed method can still effectively extract the interface to obtain the SOS distribution, thereby achieving effective aberration correction. This shows the robustness of the proposed method in noisy environments.

4. Phantom experiment

The diagram of the experimental system is shown in Fig. 7. A Q-
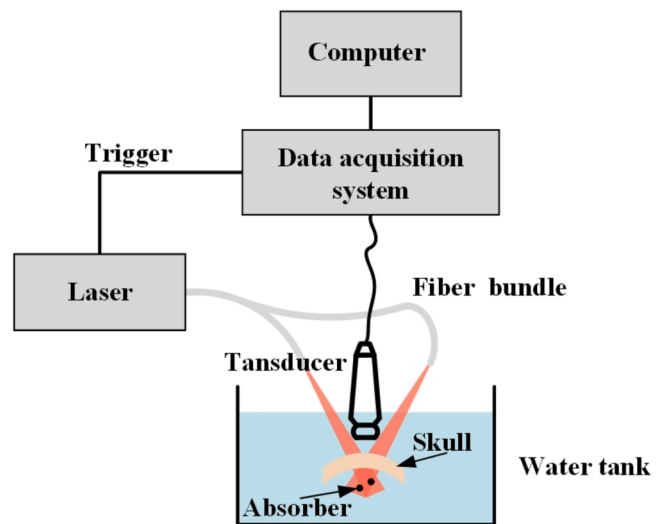
Fig. 7. The diagram of the experimental system.

switched Nd: YAG laser (OPOTEK, LLC, USA) acts as a light source to illuminate the absorber. The laser pulse with a pulse width of 4.5 ns and a pulse repetition rate of 10 Hz. The near-infrared region I (NIR-I) light with a wavelength of 750 nm was used in the experiment. The measured maximum radiant exposure on the phantom is about 15 mJ/cm^2 within

the ANSI safety limit [41]. An ultrasonic linear array transducer with a center frequency of 7.5 MHz and a −6 dB bandwidth of 80 % was used for signal acquisition. The transducer has 128 elements and a pitch of 0.3 mm. Ultrasonic transmitting and receiving work in pulse-echo mode. After the ultrasonic acquisition is completed, the photoacoustic signal acquisition is started based on a certain delay. The sampling frequency is 40 MHz.

Fig. 8 gives the phantom model and the reconstructed PA image of the absorbers in homogeneous water. In Fig. 8(a), five carbon rods (No. 1–5) fixed on a designed plate were placed in the water to simulate the absorbers. These carbon rods have a diameter of 0.5 mm. Fig. 8(a) shows a side view of the relative positions of these carbon rods. As shown in Fig. 8(b), the images of the five carbon rods are well-focused at the correct positions based on the reconstruction with 1500 m/s.

A transparent acrylic plate acted as the skull was placed over the carbon rods. The longitudinal SOS of the acrylic plate measured is 2633.9 m/s. The serious acoustic impedance mismatch between the skull and water generates strong sound refraction problems in the phantom. The thickness of the acrylic plate is 7 mm. Fig. 9(a) gives a picture of the heterogeneous model.

Fig. 9(b) is the PA image reconstructed by DAS with a constant SOS of 1500 m/s. It can be seen that the image aberration is serious in Fig. 9 (b). Fig. 9(c)-(f) present the results of SOS updated by the US. The final updated SOS map in Fig. 9(f) is consistent with the heterogeneous model. The velocity value is determined based on the priori SOS value of the material. Fig. 9(f) shows that the SOS map updated by the proposed method can effectively reflect the position where the SOS changes in a practical detection case.

With the assistance of the SOS map in Fig. 9(f), the PA images are reconstructed by the SRA method [Fig. 9(g)] and the proposed method [Fig. 9(h)], respectively. Compared with the image [Fig. 9(b)] obtained with a constant SOS, both methods have improved image quality. However, the proposed method suppresses the image distortion better than the SRA method. In comparison, the position errors of the absorber (No. 3) in the lateral direction in Fig. 9(b), (g) and (h) are 1.69 %, 0.85 %, and 0 %, respectively. The position errors in the depth direction are −13.10 %, −0.40 %, and 0 %, respectively. By comparison with Fig. 8(b), the SSIM measured is 0.39, 0.67, and 0.83. The improvement of the proposed method benefits from the phase compensation by considering the changes in velocity and direction of wave propagation.

5. *Ex-vivo* experiment

Two *ex vivo* experiments on an adult rabbit skull were carried out to examine the method in the real skull situation. The first *ex vivo* model is shown in Fig. 10(a). The skull has an irregularly curved shape and its thickness is about 2.5±1.0 mm. An iron wire with a diameter of approximately 0.7 mm was embedded in an agar block. Agar blocks were placed within the skull cavity to simulate the brain tissue. The same US-PA dual-modality system as the phantom experiment is used in this *ex vivo* experiment. The transducer used in the *ex vivo* experiment has a center frequency of 2.5 MHz and a −6 dB bandwidth of 80 %.

Fig. 10(b) gives the US-PA dual-modality image reconstructed by the DAS method with a constant SOS of 1500 m/s. In Fig. 10(b), both the US result and the PA result are seriously distorted when the skull is present due to the insufficient phase compensation. A close-up view of the PA result [dashed rectangle in Fig. 10(b)] is shown in Fig. 10(c). The position errors in the lateral and depth directions in Fig. 10(c) are −2.63 % and −3.91 %, respectively.

Fig. 10(d) is the updated SOS map obtained by the proposed method. Fig. 10(d) reveals the relative position of the skull with higher SOS in the entire imaging area. The SOS values in Fig. 10(d) are filled based on the measured prior values. Fig. 10(e) is the US-PA dual-modality image reconstructed by the proposed method. It can be seen from Fig. 10(e) that the proposed method can correct the position aberration caused by the refraction of the skull, and the shape of the absorber is more focused than that reconstructed by constant SOS [Fig. 10(b)]. In the close-up view of the PA result in Fig. 10(e) [Fig. 10(f)], the position errors in the lateral and depth directions in Fig. 10(c) are reduced to −1.32 % and 0.98 %, respectively. The SSIM measured in Fig. 10(b) and (e) is 0.60 and 0.79. These results show that the proposed method has the potential to be used for aberration correction of transcranial PA imaging.

The second *ex vivo* experiment with two intersecting hairs is imaged and the actual picture is shown in Fig. 11(a). The hairs were set at a distance of about 20 mm from the skull. For comparison, the result without a skull present is first given in Fig. 11(b). Fig. 11(c) and (d) are the imaging results before and after correction by the proposed method when there is a skull in the propagation path. It can be seen from the blue dotted box in the results that the proposed method can effectively compensate for refraction aberration. By comparing with the result without aberration [Fig. 11(b)], the SSIM obtained by the proposed method is 0.53, which is higher than that of 0.48 in Fig. 11(c). This shows that the result obtained by the proposed method is more consistent with the reality than that obtained before correction. However,
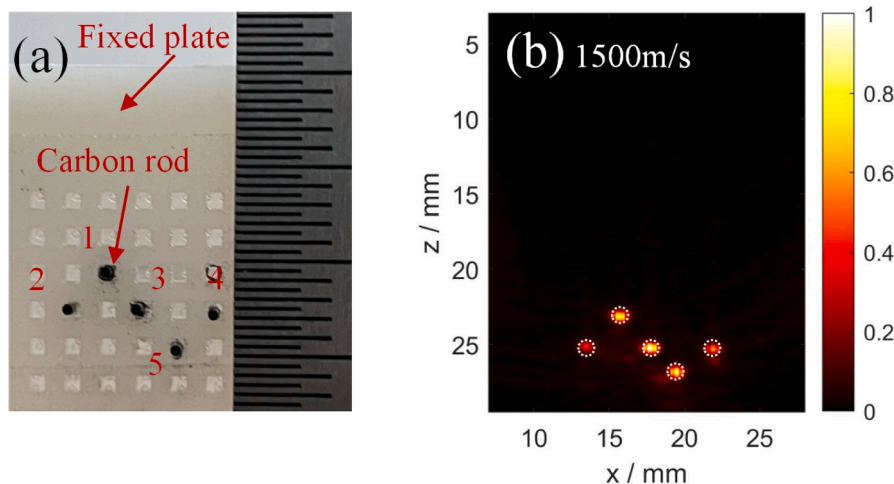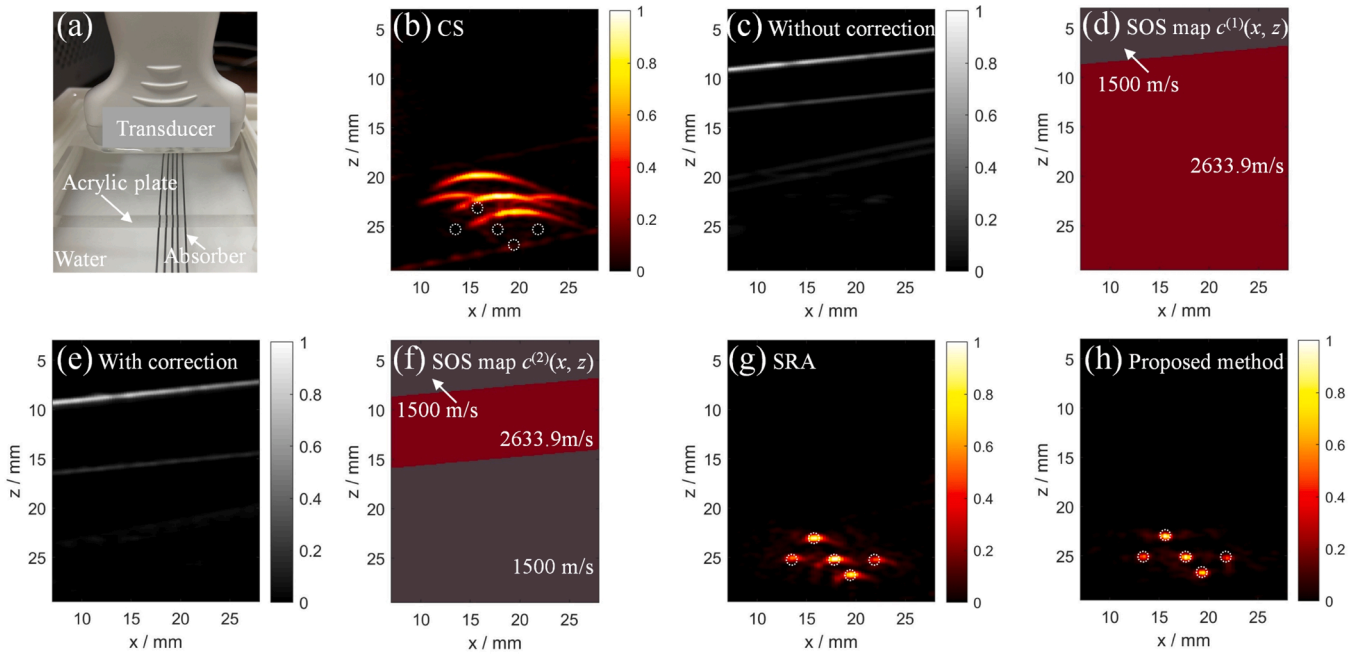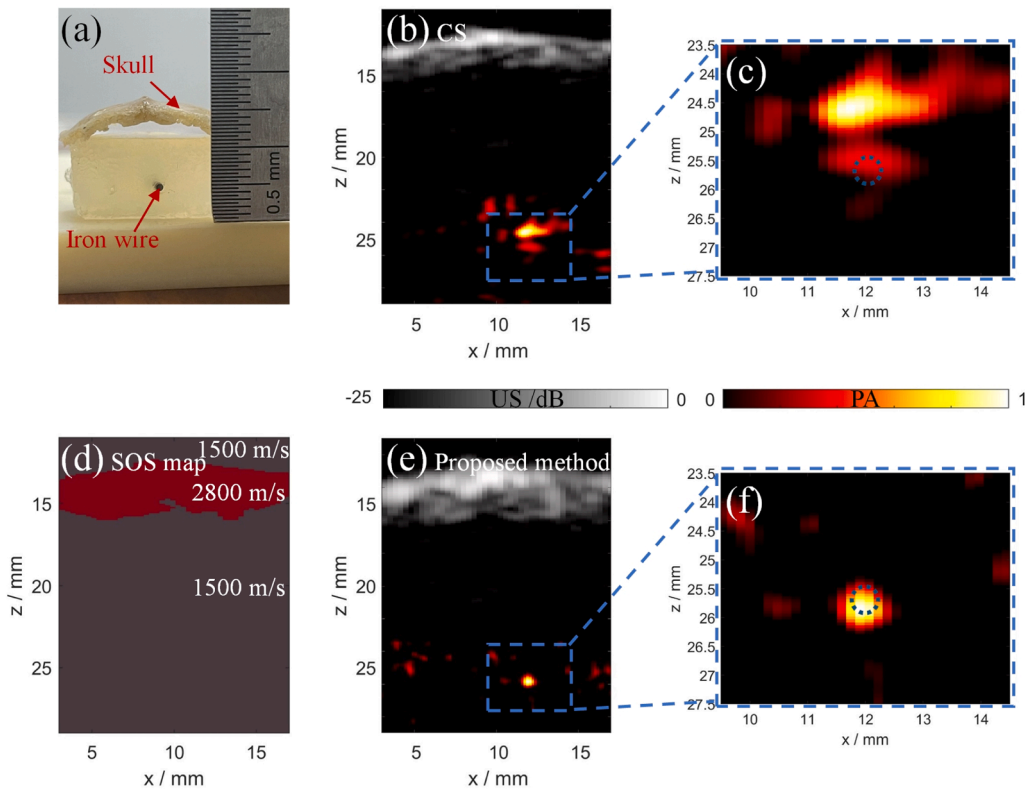

Fig. 8. Phantom experiment in water. (a) A picture of a side view of the phantom. (b) PA image reconstructed by using DAS at a constant speed of 1500 m/s. White dashed circles reveal the real position of absorbers.

Fig. 9. Phantom experiment with the acrylic plate present. (a) A picture of the heterogeneous model, where an acrylic plate is placed between the transducer and the absorbers. (b) PA image reconstructed by using DAS at a constant speed of 1500 m/s. (c) US image reconstructed by using DAS at 1500 m/s. (d) Updated SOS map $c^{(1)}(x, y)$ according to the interface of (c). (e) US image reconstructed with the SOS map of (d). (f) Updated SOS map $c^{(2)}(x, y)$ according to the interface of (e). (g) PA image reconstructed by SRA method with the SOS map of (f). (h) PA image reconstructed by the proposed method with the SOS map of (f). White dashed circles in the PA image reveal the real position of absorbers.

Fig. 10. *Ex-vivo* rabbit skull experiment. (a) A picture of the skull model with an absorber. (b) US-PA dual-modality image reconstructed by using DAS at a constant speed of 1500 m/s. (c) The close-up view of the absorber in (b). (d) Updated final SOS map based on the proposed method. (e) US-PA dual-modality image reconstructed by the proposed method with the SOS map of (d). (f) The close-up view of the absorber in (e). The dashed rectangle outlines the region to be enlarged. Dashed circles in the PA image reveal the real position of the absorber.
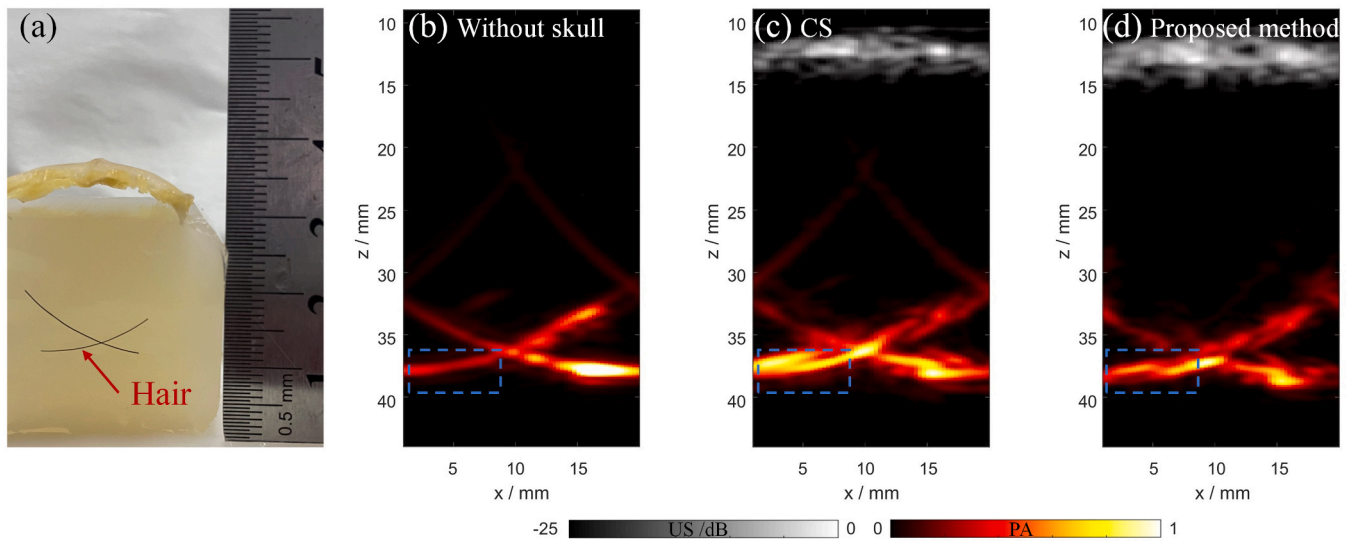
Fig. 11. Ex-vivo rabbit skull experiment with intersecting hairs. (a) A picture of the skull model with intersecting hairs. (b) PA image without skull present reconstructed by using DAS at a constant speed of 1500 m/s. (c) US-PA dual-modality image with skull present reconstructed at a constant speed of 1500 m/s. (d) US-PA dual-modality image with skull present reconstructed by the proposed method. The blue dashed rectangle outlines the region to be compared.

some artifacts in the image caused by the scattering, multiple reflections, etc. in the skull, can not be effectively handled by the proposed method which is based on the phase compensation by considering the refraction.

6. Discussion

In this work, a method combining the US and PA imaging based on the angular spectrum is proposed to address the PA image aberration. The wavefront phase distortion caused by the skull refraction can be effectively compensated using the proposed method. Results of simulations and experiments demonstrate the effectiveness of the proposed method. The reconstruction of the region of interest depends on the continuous shift of the angular spectrum along the depth direction. The accuracy of reconstruction depends on the Δz during shift. A smaller Δz can bring better depth resolution, but this comes at the expense of reconstruction speed. Generally, $\Delta z = \lambda/4$ is enough to obtain better results and imaging speed trade-off.

In terms of computational cost, for the 2400×128 size of US and PA signals, the average time consumption of the proposed method is ~5.37 s of the complete processing from the SOS distribution reconstruction by US to aberration correction for PA imaging. The average time consumption of the SRA method is ~169.26 s for correction. The image reconstruction is performed in Matlab R2023b on the CPU with Intel Core i7–1165G7. By using a higher-performance GPU, the computational efficiency in the proposed method will be further improved, which is expected to achieve real-time imaging.

The proposed method relies on prior knowledge of SOS distribution within the imaging region, which is obtained from US images in this study. While x-ray computerized tomography and magnetic resonance imaging offer more precise medium properties, the US has the advantages of simple integration to PA and without radiation exposure. The combination of US and PA can obtain the US-PA dual-modality image that can simultaneously reflect structural and functional information. In this work, US imaging operates in pulse-echo mode for rapid acquisition. Employing advanced acquisition modes, such as composite plane wave acquisition, may enhance US image quality for more accurate skull distribution mapping, but at the expense of time and storage resources.

The SOS estimation can also be recovered by the full-wave inversion (FWI) method using ultrasound [42,43]. The FWI method can obtain the SOS distribution with a high resolution through iteration. However, the

result obtained by the FWI method is very dependent on the input initial velocity model. It is expected to successfully iterate the accurate SOS distribution when the initial model is 90 % close to the real model. The proposed method can effectively and quickly reconstruct the acoustic impedance mismatch interface, that is, it has the potential to quickly provide a more accurate initial SOS model for full-wave inversion input in the future.

The proposed method can be easily extended to the 3D wave equation, though it is derived based on the 2D wave equation in this work. At this time, 3D Fourier transform and piecewise integration are needed in 3D cases. Then, consistent with the 2D case, the wave field is extrapolated layer-wise along the depth direction.

The rabbit skulls used in this work are relatively thin compared to adult human skulls. Higher laser energy and longer wavelengths should be utilized to verify the performance of the proposed method on human skulls. Additionally, employing a transducer with a lower center frequency, such as <1 MHz, could enhance signal reception, particularly for low-frequency signals attenuated by the skull, in contrast to the 2.5 MHz transducer utilized in this study.

Although this work assumes the skull layer to be a uniform medium, the real skull experiment verifies the effectiveness of the proposed method. As this work focuses on longitudinal wave refraction, artifacts arising from multiple interlayer reflections, waveform conversion, and scattering remain unexplained by the proposed method. Addressing these issues in future research will be crucial for achieving high-quality and accurate PA images.

7. Conclusion

In summary, a method is proposed in this work to effectively compensate for PA image aberration caused by the refraction of the skull. This method updates the SOS distribution by simply iteratively correcting the US image, thereby assisting the phase compensation for aberration correction in PA reconstruction. Aberration correction in this proposed method avoids the complex calculations of refraction angles and paths in the time domain, keeping computational complexity manageable. In this method, not only the aberration in PA images but also the aberration in US images can be corrected based on the angular spectrum theory. Thus, owing to the aberration-free US-PA dual-modality images, the proposed method has the potential to be employed for structural and functional transcranial imaging in humans.

CRediT authorship contribution statement

Xiaojun Liu: Writing – review & editing, Validation, Supervision, Data curation. **Chao Tao:** Writing – review & editing, Supervision, Methodology, Data curation, Conceptualization. **Yingjie Feng:** Writing – review & editing, Validation, Methodology, Investigation. **Qiuqin Mao:** Writing – review & editing, Writing – original draft, Validation, Software, Methodology, Conceptualization.

Declaration of Competing Interest

No conflict of interest exists in the submission of this manuscript.

Acknowledgments

Data availability

Data will be made available on request.

References

[1] S. Hu, K. Maslov, V. Tsytsarev, L.V. Wang, Functional transcranial brain imaging by optical-resolution photoacoustic microscopy, J. Biomed. Opt. 14 (4) (2009) 040503.

[2] J. Kang, X. Liu, S. Cao, S.R. Zeiler, E.M. Graham, E.M. Boctor, R.C. Koehler, Transcranial photoacoustic characterization of neurovascular physiology during early-stage photothrombotic stroke in neonatal pigletsin vivo, J. Neural Eng. 18 (6) (2022) 065001.

[3] R. Manwar, K. Kratkiewicz, K. Avanaki, Investigation of the effect of the skull in transcranial photoacoustic imaging: a preliminary Ex vivo study, Sensors 20 (15) (2020) 4189.

[4] L. Nie, X. Cai, K. Maslov, A. Garcia-Uribe, M.A. Anastasio, L.V. Wang, Photoacoustic tomography through a whole adult human skull with a photon recycler, J. Biomed. Opt. 17 (11) (2012) 110506.

[5] J. Ylitalo, J. Koivukangas, J. Oksman, Ultrasonic reflection mode computed tomography through a skullbone, IEEE Trans. Biomed. Eng. 37 (11) (1990) 1059–1066.

[6] C. Li, A. Aguirre, J. Gamelin, A. Maurudis, Q. Zhu, L.V. Wang, Real-time photoacoustic tomography of cortical hemodynamics in small animals, J. Biomed. Opt. 15 (1) (2010) 010509.

[7] X. Wang, Y. Pang, G. Ku, X. Xie, G. Stoica, L.V. Wang, Noninvasive laser-induced photoacoustic tomography for structural and functional in vivo imaging of the brain, Nat. Biotechnol. 21 (7) (2003) 803–806.

[8] A. Paul, S. Mallidi, U-Net enhanced real-time LED-based photoacoustic imaging, Journal of Biophotonics (2024) e202300465.

[9] Y. Yu, T. Feng, H. Qiu, Y. Gu, Q. Chen, C. Zuo, H. Ma, Simultaneous photoacoustic and ultrasound imaging: a review, Ultrasonics 139 (2024) 107277.

[10] T. Tarvainen, B. Cox, Quantitative photoacoustic tomography: modeling and inverse problems, J. Biomed. Opt. 29 (S1) (2024) S11509.

[11] P. Beard, Biomedical photoacoustic imaging, Interface Focus 1 (4) (2011) 602–631.

[12] C. Kim, T.N. Erpelding, L. Jankovic, M.D. Pashley, L.V. Wang, Deeply penetrating in vivo photoacoustic imaging using a clinical ultrasound array system, Biomed. Opt. Express 1 (1) (2010) 278–284.

[13] J. Yao, L.V. Wang, Photoacoustic brain imaging: from microscopic to macroscopic scales, Neurophotonics 1 (1) (2014) 011003.

[14] X. Yang, Y.H. Chen, F. Xia, M. Sawan, Photoacoustic imaging for monitoring of stroke diseases: a review, Photoacoustics 23 (2021) 100287.

[15] L. Mohammadi, H. Behnam, M.R.N. Avanaki, Skull's photoacoustic attenuation and dispersion modeling with deterministic ray-tracing: towards real-time aberration correction, Sensors 19 (2) (2019).

[16] X. Wang, Y. Luo, Y. Chen, C. Chen, L. Yin, T. Yu, W. He, C. Ma, A. Skull-Removed, Chronic cranial window for ultrasound and photoacoustic imaging of the rodent brain, Front. Neurosci. 15 (2021) 673740.

[17] B. Liang, W. Liu, Q. Zhan, M. Li, M. Zhuang, Q.H. Liu, J. Yao, Impacts of the murine skull on high-frequency transcranial photoacoustic brain imaging, J. Biophotonics 12 (7) (2019) 1–10.

[18] B. Liang, S. Wang, F. Shen, Q.H. Liu, Y. Gong, J. Yao, Acoustic impact of the human skull on transcranial photoacoustic imaging, Biomed. Opt. Express 12 (3) (2021) 1512.

[19] C. Huang, L. Nie, R.W. Schoonover, Z. Guo, C.O. Schirra, M.A. Anastasio, L.V. Wang, Aberration correction for transcranial photoacoustic tomography of primates employing adjunct image data, J. Biomed. Opt. 17 (6) (2012) 066016.

[20] S. Na, X. Yuan, L. Lin, J. Isla, D. Garrett, L.V. Wang, Transcranial photoacoustic computed tomography based on a layered back-projection method, Photoacoustics 20 (2020) 100213.

[21] X. Lin, M. Sun, Y. Liu, Z. Shen, Y. Shen, N. Feng, Variable speed of sound compensation in the linear-array photoacoustic tomography using a multi-stencils fast marching method, Biomed. Signal Process. Control 44 (2018) 67–74.

[22] D. Modgil, M.A. Anastasio, P.J.L. Rivière, Image reconstruction in photoacoustic tomography with variable speed of sound using a higher-order geometrical acoustics approximation, J. Biomed. Opt. 15 (2) (2010) 021308.

[23] J. Jose, R.G.H. Willemink, W. Steenbergen, C.H. Slump, T.Gv Leeuwen, S. Manohar, Speed-of-sound compensated photoacoustic tomography for accurate imaging, Med. Phys. 39 (12) (2012) 7262–7271.

[24] H. Estrada, J. Rebling, J. Turner, D. Razansky, Broadband acoustic properties of a murine skull, Phys. Med. Biol. 61 (5) (2016) 1932–1946.

[25] M. Dantuma, F. Lucka, S.C. Kruitwagen, A. Javaherian, L. Alink, R.P.Pv Meerdervoort, M. Nanninga, T.J.P.M.Ot Root, B.D. Santi, J. Budisky, G. Bordovsky, E. Coffy, M. Wilm, T. Kasponas, S.H. Aarnink, L.Fd Geus-Oei, F. Brochin, T. Martinez, A. Michailovas9, W.M. Kobold, J. Jaros, J. Veltman, B. Cox, S. Manohar, Fully three-dimensional sound speed-corrected multi-wavelength photoacoustic breast tomography, arXiv preprint arXiv:2308.06754 (2023).

[26] Y. Aborahama, K. Sastry, M. Cui, Y. Zhang, Y. Luo, R. Cao, L.V. Wang, De-aberration for transcranial photoacoustic computed tomography through an adult human skull, arXiv preprint arXiv:2404.05937 (2024).

[27] J. Poudel1, S. Na, L.V. Wang, M.A. Anastasio, Iterative image reconstruction in transcranial photoacoustic tomography based on the elastic wave equation, Phys. Med. Biol. 65 (2020) 055009.

[28] J. Poudel, M.A. Anastasio, Joint reconstruction of initial pressure distribution and spatial distribution of acoustic properties of elastic media with application to transcranial photoacoustic tomography, Inverse Probl. 36 (2020) 124007.

[29] K. Mitsuhashi, J. Poudel, T.P. Matthews, A. Garcia-Uribe, L.V. Wang, M. A. Anastasio, A forward-adjoint operator pair based on the elastic wave equation for use in transcranial photoacoustic computed tomography, Siam J. Imaging Sci. 10 (4) (2017) 2022–2048.

[30] F. Zhang, J. Zhang, Y. Shen, Z. Gao, C. Yang, M. Liang, F. Gao, L. Liu, H. Zhao, F. Gao, Photoacoustic digital brain and deep-learning-assisted image reconstruction, Photoacoustics 31 (2023) 100517.

[31] Y. Gao, W. Xu, Y. Chen, W. Xie, Q. Cheng, Deep learning-based photoacoustic imaging of vascular network through thick porous media, IEEE Trans. Med. Imaging 41 (8) (2022) 2191–2204.

[32] X.L. Deán-Ben, D. Razansky, A practical guide for model-based reconstruction in optoacoustic imaging, Front. Phys. 10 (2022) 1028258.

[33] J.W. Goodman, Introduction to Fourier optics, 1969.

[34] T. Tang, C. Shen, L. Huang, Propagation of acoustic waves and determined radiation effects on axisymmetric objects in heterogeneous medium with irregular interfaces, Phys. Fluids 36 (1) (2024) 012023.

[35] A. Rosenthal, V. Ntziachristos, D. Razansky, Acoustic inversion in optoacoustic tomography: a review, Curr. Med. Imaging Rev. 9 (4) (2013) 318–336.

[36] G.F. Margrave, R.J. Ferguson, Wavefield extrapolation by nonstationary phase shift, Geophysics 64 (4) (1999) 1067–1078.

[37] B.E. Treeby, B.T. Cox, K-wave: matlab toolbox for the simulation and reconstruction of photoacoustic wave fields, J. Biomed. Opt. 15 (2) (2010) 021314.

[38] D. Lévesque, A. Blouin, C. Néron, J.-P. Monchalin, Performance of laser-ultrasonic F-SAFT imaging, Ultrasonics 40 (2002) 1057–1063.

[39] Y. Slobodkin, O. Katz, Computational wave-based photoacoustic imaging through an unknown thick aberrating layer, Photoacoustics 36 (2024) 100584.

[40] Z. Wang, A.C. Bovik, H.R. Sheikh, E.P.Simoncelli Image, quality assessment: from error visibility to structural similarity, IEEE Trans. Image Process. 13 (4) (2004) 600–612.

[41] American National Standard for Safe Use of Lasers ANSI Z136.1–2000, American National Standards Institute, Inc., New York, NY (2000).

[42] F. Lucka, M. Pérez-Liva, B.E. Treeby, B.T. Cox, High resolution 3D ultrasonic breast imaging by time-domain full waveform inversion, Inverse Probl. 38 (2022) 025008.

[43] L. Guasch, O. Calderón Agudo, M.X. Tang, P. Nachev, M. Warner, Full-waveform inversion imaging of the human brain, npj Digit. Med. 3 (28) (2020).

Qiuqin Mao is currently a Ph.D. candidate student in the Ministry-of-Education Key Laboratory of Modern Acoustics, Department of Physics, Collaborative Innovation Center of Advanced Microstructures of Nanjing University. She received her B.S. degree in 2018 from Nanjing University of Information Science and Technology. Her research interests are in photoacoustic imaging and biomedical imaging.

Yingjie Feng is currently a Ph.D. candidate student in the Ministry-of-Education Key Laboratory of Modern Acoustics, Department of Physics, Collaborative Innovation Center of Advanced Microstructures of Nanjing University. He graduated from Nanjing University with a B.S. degree in 2023. His research focusses on photoacoustic tomography and imaging algorithms.

Chao Tao was born in Zhenjiang, Jiangsu, China, in 1978. He received the B.S. degree in electronic engineering and the Ph.D. degree in acoustics from Nanjing University, China, in 2000 and 2004, respectively. From 2005–2009, he visited the Department of Surgery in University of Wisconsin-Madison (USA) as a Postdoctoral Research Fellow. Since 2009, he works as an Associate Professor and Full Professor at Institute of Acoustics in Nanjing University, China. His professional research interest is in biomedical imaging. He has studied the ultrasound/photoacoustic imaging and developed several new imaging systems. He also applied these systems to brain imaging, microvasculature imaging, dental imaging, and so on. Dr. Tao has published over 100 peer-reviewed papers in these areas.

Xiaojun Liu received the B.S., M.S., and Ph.D. degree in acoustics from Nanjing University, China, and a doctorate in applied physics (engineering) from Nagoya University, Japan. He was a postdoctoral researcher at Nagoya University, Japan, a special researcher at Japan Society for the Promotion of Science (JSPS), a senior researcher at Japan Science and Technology Agency (JST), and a visiting professor at Nagoya University. He is currently a professor at Nanjing University and is the chairman of Jiangsu Acoustics Society. His research interests are photoacoustic and acoustic metamaterials.